Acta Astronautica 159 (2019) 517–526

Contents lists available at ScienceDirect

Acta Astronautica

journal homepage: www.elsevier.com/locate/actaastro

A compact C-Band CP-SAR microsatellite antenna for Earth Observation

Katia N. Urata[a,*], Josaphat T. Sri Sumantyo[a], Cahya E. Santosa[a,b], Tor Viscor[c]

[a] Center for Environment Remote Sensing, Chiba University, Japan
[b] National Institute of Aeronautics and Space of Indonesia, Indonesia
[c] V-Space, Japan

ARTICLE INFO

Keywords:
Microsatellite
SAR
Deployable
Reflector
Synthetic aperture radar
Antenna
Circular polarization
C-band

ABSTRACT

This work describes the development of a compact Circularly Polarized SAR C-band antenna system and the design considerations suitable to use on small spacecrafts. To reduce size and weight of the small spaceborne SAR, we utilize a lightweight deployable parabolic mesh reflector and operate at low Earth orbital altitudes. The antenna is a wrap-rib center-fed parabolic reflector with dedicated receiving and transmitting feeds. Antenna requirements are: center frequency of 5.3 GHz with bandwidth of 400 MHz and circular polarization with axial ratio better than 3 dB. Simulation of the parabolic reflector and effects of different structural elements to the main radiation pattern is analyzed, which include ribs, struts, feed blockage and mesh surface. A research model of the parabolic reflector was constructed. Surface verification was realized using two different approaches, one using a laser distance meter along ribs and the other using 3D scanning of the reflector surface, with respective surface accuracy of 1.92 mm and 3.86 mm RMS. Near-field antenna measurements of the deployable reflector mesh antenna was realized for final antenna validation, presenting good agreement with the simulation results. Future work comprises of prototyping and testing of the full polarimetric feed assembly.

1. Introduction

1.1. Background on SAR spacecrafts and small satellites

Synthetic Aperture Radar (SAR) technology has been widely used in Earth Observation applications, as it can provide unique information independent of cloud coverage and during night time. With the recent miniaturization of technological components, it is nowadays possible to achieve significantly reduced size of payload and bus systems [1]. Constellations of small satellites carrying scientific or commercial payloads provide fast responses and near real-time ground monitoring [2]. Many of such satellites carry small payloads as optical cameras or radio receivers, with spacecraft mass ranging from less than a kilogram to few hundred kilograms. However, when it comes to spaceborne SAR, mostly due to the large antenna sizes and high transmission power required, reducing the total spacecrafts mass becomes a very challenging task. Consequently, the bulky payloads and high costs result in SAR missions being commonly sponsored by governmental space agencies. Therefore, up to this date, the number of compact SAR missions with mass of few hundred kilograms are very limited. Moreover, there is a strong social demand to realize small and affordable SAR satellites for fast responses and all-weather monitoring. Such needs are especially important in the Southeast Asian countries, which are often covered by clouds, limiting observation with optical satellites.

Fig. 1a depicts past, existing and future spaceborne SAR missions, relating total spacecraft mass and respective ground resolution, for Noise Equivalent Delta Sigma σ^0_{NE} = -20 dB. For each SAR frequency band, there is a visible barrier in size, performance and, consequently, costs to be able to set up affordable SAR constellations. The miniaturization trend in spaceborne SAR is clearly visible in the high frequency bands, but breaking the ton-sized category is still challenging in the low frequencies, namely L- and C-bands. Low SAR frequencies can provide unique ground surface scattering information, a capability not achieved with higher microwave frequencies, but respective antenna dimensions are inherently large. That is why the very few existing compact spaceborne SAR missions operate in the X- or S-bands, as such antennas occupy low volume and are easier to stow. Some examples are the X-band TECSAR (Israel, 300 kg) [3], pioneer in showing that a SAR payload could be flown on smaller satellites, and the recently launched X-band microsat SAR ICEYE-X1 (Finland, 70 kg) [4], a promising proof-of-concept prototype for future planned constellation.

Currently, Chiba University and the Indonesian National Institute of Aeronautics and Space (LAPAN) are developing a C-band SAR microsatellite for Earth Observation, namely LapanChibasat mission, as part of a technology demonstrator for small spaceborne SAR systems. Table 1 describes the considered remote sensing applications covered

* Corresponding author. Center for Environment Remote Sensing, Chiba University, Yayoi 1-33, Inage, Chiba, 263-8522, Japan.
E-mail address: afya9593@chiba-u.jp (K.N. Urata).

https://doi.org/10.1016/j.actaastro.2019.01.030
Received 22 November 2018; Received in revised form 16 January 2019; Accepted 23 January 2019
Available online 05 February 2019

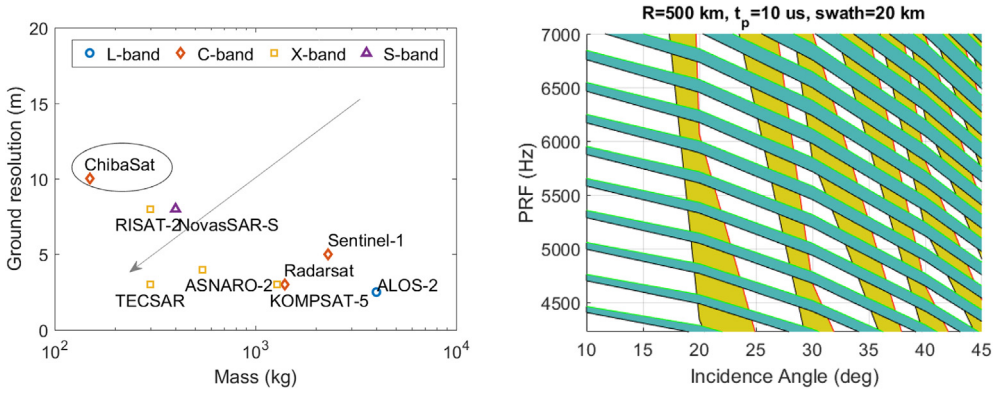

Fig. 1. (a) Trends in miniaturization of past, current and future sapaceborne SAR missions: spacecraft mass versus range resolution for σ^0_{NE} = -20 dB. (b)Dependency of usable PRFs (white area) as incidence angles vary. Unavailable PRF values due to blind ranges and nadir returns are depicted in yellow and blue. (For interpretation of the references to color in this figure legend, the reader is referred to the Web version of this article.)

Table 1
Remote sensing applications of the C-band microsat mission.

Application	Detail
Land	Forest classification
	Land deformation
	Paddy field extraction
	Wetland extraction
	Mangrove area mapping
Ocean	maritime traffic
	oil spill
	ocean waves
Cryosphere	Icebergs

by the mission. A new concept of a 150-kg-class microsatellite Circularly Polarized SAR is proposed, composed of a compact C-band SAR payload, allowing for piggy-back launch opportunities for the mission. Main strategies for weight and volume reduction are based on a deployable and lightweight SAR antenna, a compact SAR RF system inherited from an airborne-base system previously tested [5], and the use of a low Earth orbit. A primary goal is to demonstrate basic SAR acquisition, showing that a C-band SAR mission can be performed with a microsatellite, and therefore, making SAR data more affordable for the global remote sensing communities in the future.

1.2. Motivation for deployable reflector antenna

The SAR antenna is one of the design drivers of SAR platforms. It plays an important role with regards to the final imaging performance, as antenna gain, cross-polarization and side lobe levels (SLL) directly affect the SAR data quality. For the implementation of a small C-band SAR satellite, a lightweight high-gain antenna that occupies low stowage space is the main challenge. Such requirements dictates the adoption of deployable antennas. There are promising ongoing developments on deployable inflatable antennas, but difficulties in controlling gas pressure still poses critical challenges, and thus deemed not suitable for our requirements. A common choice for SAR antennas is deployable active phased array antennas, as in the 10 m-long L-band antenna onboard ALOS-2 [6]. However, such antenna types are usually heavy, expensive and with complex design.

On the other hand, reflector antennas are one of the most commonly used solutions for high-gain spacecraft antennas [2], as they provide high efficiency and can support any polarization. Deployable mesh antenna reflectors have proven to be a venerable product for low frequency communications and radar applications where high gain is required. But there have been very few scientific missions that have successfully adopted deployable reflectors, such as the 6-m large deployable mesh reflector antenna for SMAP (Soil Moisture Active Passive) mission [7,8], with most being extensively used for commercial or military applications [2,3]. Up to date, all flown deployable reflectors have been developed for large spacecrafts, which makes directly scaling down to microsatellite dimensions not possible, since mesh parameters (density, coating, among others) are driven by the deployment mechanism elements and RF requirements.

1.3. Motivation for circularly polarized SAR

Earth Observation spaceborne SAR systems are conventionally linearly-polarized, though there are many benefits of circularly-polarized sensors [9]. Circular polarization has the advantage of minimizing the ionospheric effect known as Faraday rotation, which degrades linearly polarized waves most severely in the frequencies below 1.2 GHz. Although Faraday rotation is less prominent in the C-band, the use of circular polarization reduces effects of antenna misalignments and multipath propagation, improving the received signal. Circular polarization is typically used in satellite communication links, but its use in spaceborne SAR systems for remote sensing has not been much explored. The main reason is difficulty in making antenna systems that comply with the strict requirements of circular polarization, such as antennas with very good axial ratio.

In polarimetric SAR, transmitting in circular or tilted linear polarization has gained popularity over the years as it overcomes existing drawbacks in the conventional polarimetric linear polarized SAR, the so-called compact polarimetric or pseudo quad-pol SAR [10]. The drawback is that, although suitable for some key applications, compact SAR data cannot replicate all aspects of full polarimetric imagery.

Recently, a SAR mode that adopts circular polarization signals in transmission while receiving both polarizations has been proposed [9], and its concept referred to CP-SAR (Patent Pending 2014–214905). Application of a ground based full-polarimetric CP-SAR on rice phenology monitoring has been demonstrated [11], showing adequate classification capability of rice paddies.

The C-band microsat is designed to support full polarimetric CP-SAR for concept demonstration, but to avoid too large data amounts it should operate mostly in one polarization, that is, transmitting either left-hand-circular polarization (LHCP) or right-hand-circular polarization (RHCP), and receiving both. In order to guarantee a high degree of circularly polarized scattered waves, the microsat CP-SAR must must consider look angles below 50°, as up to this angle, the polarization of scattered waves presents axial ratio under 3 dB [9]. Apart from being a technology demonstrator, the microsat's main mission is to support further research on elliptically polarized scattering for remote sensing

applications, aiming for the development of end-user products.

1.4. Motivation for low earth orbits

Lowering orbital altitudes is a clear advantage for small sats, as it directly reduces the minimum antenna area that complies with the pulse repetition frequency (PRF) constrains. Power requirements and cross track resolution are also improved in lower orbits [12]. The minimum antenna area $A_{min}$is a function of orbital height R, incidence angle θ and platform velocity v_{st}, referenced in Equation (1).

$$A_{min} \geq \frac{4v_{st}R\lambda tan(\theta)}{c} \quad (1)$$

Additionally, a reduction on the antenna dimensions as much as possible to fit the launcher envelope is mandatory. Therefore, an orbit height as low as possible is advantageous for the CP-SAR microsat. On the other hand, orbital altitudes lower than 500 km are subjected to atmospheric drag, considerably reducing the mission life time. Accounting the requirements of the Indonesian and Japanese partners, the investigations will concentrate on orbits with height between 400 and 550 km, accepting a shorter mission life span of at least 1 year. Therefore, the basis for the SAR sensor design was chosen to be at a height over ground of 500 km.

This work presents the main design considerations for a compact SAR antenna, simulation and validation of the parabolic reflector antenna. Antenna pattern simulations were performed with the full wave simulation software 2018 CST Studio [13]. Due to the high degree of signal purity required for the feed pattern, the complete design and verification of the feed assembly will be addressed in a separate work package. Simulations and antenna measurements will consider a single feed antenna element. Future work shall concentrate in the development and performance verification of the feed assembly.

This document is organized as follows: Chapter 2 describes the main considerations for the design of the deployable mesh reflector antenna; Chapter 3 describes the antenna effective gain estimation; Chapter 4 presents methods for the verification of reflector surface accuracy and subsequent results achieved; Chapter 5 concludes with a summary of the current study and an outlook to future work.

2. Deployable mesh antenna design

2.1. SAR considerations

In a SAR system, the antenna size must be determined at an early stage of the design, as antenna length and width define the half-power beamwidth (3 dB BW) of the antenna pattern, from which many other SAR parameters are derived.

Volume constraints from the launcher envelope allow a maximum antenna diameter of 3.6 m, which corresponds to maximum swath width of 15 km for an altitude of 500 km and single-fed parabolic dish. Larger swaths can be achieved by either feed defocusing or adding more feed elements.

A 3.6-m antenna size gives a $PRF_{min}$of 4.2 kHz, and defines a range of valid PRFs and subsequent SAR system parameters. Fig. 1b plots usable PRF values (white area) as a function of incidence angle for a 3.6 m-diameter parabolic antenna, accounting eclipsing from transmitter pulse (yellow) and nadir echos (blue). Therefore, non-interference PRF values are in the range of 4.2–7.5 kHz for look angles from 15°to 35°, corresponding to an access area of 216 km on both sides of the nadir track. However, in full polarimetric mode, the PRF must be doubled, leading to a useful range of 8.4–15 kHz. Corresponding calculated noise, namely Ambiguity Signal Ratio (ASR), remains below −18 dB when considering targets with uniform reflectivity. A standard value of −20 dB for image quality Noise Equivalent Sigma Nought (NESZ) can also be achieved with an average transmitted power of 100 W and a ground resolution of 5 m. Therefore, a 3.6 m diameter sized antenna in combination with low orbit would allow good SAR sensitivity with reasonable power budget. A summary of the mission and antenna's specifications can be seen in Table 2.

Table 2
Mission and antenna specifications.

Mission	Specification
Altitude	400–550 km
Orbit	sun-synchronous polar inclination of 97. 6°
SAR Modes	stripmap, spotlight
Coverage	Japan, Indonesia
Frequency	C-band (5.3 GHz 400 MHz bandwidth)
Polarization	transmit LHCP/RHCP receive LHCP + RHCP
Spatial resolution	5–15 m
Swath width	>15*km*
Look angle	15° − 35°
Bus Size	80 × 80 × 85 cm
Total mass	<150 kg
Peak power	1500 W
Duty cycle	10%
PRF	4.2–15 kHz
NESZ	< − 20 dB
ASR	< − 18 dB
Chirp Pulse	10–20 μs
Antenna	Specification
center wavelength	5.6 cm
Gain	> 40 dBic
Polarization	LHCP and RHCP
surface accuracy	< 3.5 *mm RMS*
Axial ratio	> 3 dB
Side lobe level	>20 *dBic*
Stowed size (m)	0.85 × 0.85 x 1.3
Deployed size (m)	3.6 × 0.65 (depth)
Total mass (kg)	<15

Next, details on the design of the parabolic reflector antenna will be discussed.

2.2. Antenna configuration

Among the different types of reflector configurations, a primary center-fed parabolic type was chosen. Other reflector configurations were considered, but they would either present more complex design or not satisfy the CP-SAR requirements. For instance, having an offset feed could avoid feed blockage, but at the cost of decrease of CP signal purity and increased design complexity of the deployment mechanism; a C-band Cassegrain configuration could significantly improve feed illumination efficiency but would require a too large subreflector, posing a problem in terms of volume constraints and signal purity. Hence, aiming for a simple configuration suitable for the system specifications, a primary-fed parabolic configuration was chosen. Careful feed design to minimize feed blockage achieving desired level of signal purity is then required for optimum performance.

The antenna system consists of the following elements: feed assembly, comprising of switchable LHCP and RHCP receiving and transmitting antennas, 6 aluminum support struts, and a parabolic reflector, composed of 24 ribs, a solid aluminum center plate and thin mesh layer covering the rest of the surface. Fig. 2a and b illustrate the deployable antenna. The fairing space limited the parabolic focal distance to f_d = 1.3m, resulting in f/D parameter of 0.363. The deployable reflector's total weight is 15 kg, with dimensions of 3.6 m by 0.65 m depth when deployed, and 0.85 m by 0.85 m by 1.3 m when stowed.

Since the sensor has no electronic beam steering, the whole satellite must be pointed in the necessary position for pointing to the desired target.

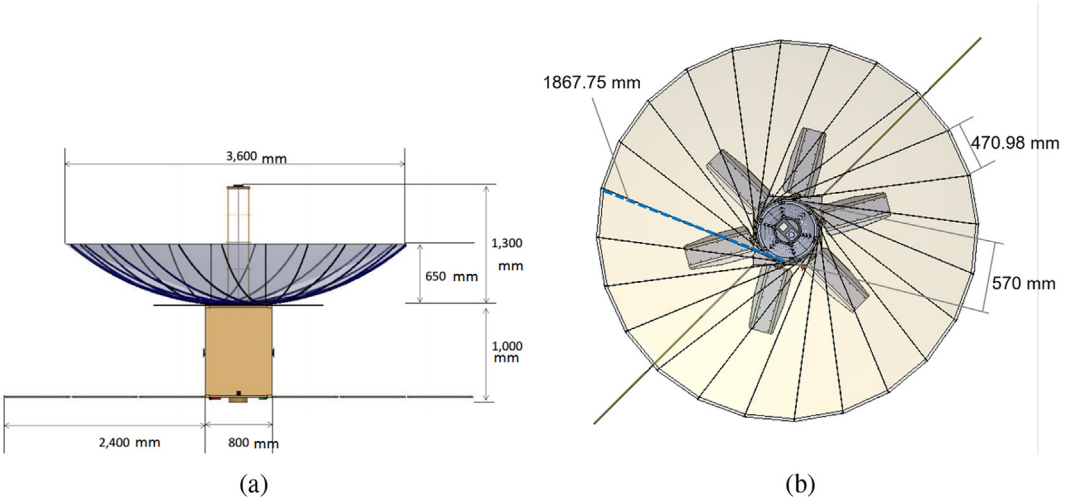

Fig. 2. Configuration of deployable mesh parabolic reflector: (a) profile and (b) top view.

2.3. Feed antenna

The parabolic reflector is validated using a single feed antenna, namely a previously demonstrated CP-SAR microstrip patch antenna [14], characterized by a wide bandwidth and small dimensions (42 mm × 65 mm x 3.2 mm). Its compact size and good performance within operational bandwidth make it a suitable candidate for the center-fed parabolic reflector. Its layout and measured performance can be seen in Figs. 3–5. A summary of measured parameters are resumed in Table 3.

2.4. Deployment structure

The stow volume dictated the type of mechanical deployment scheme to be used. The antenna is a wrap-rib type, and a mesh layer is attached to the radial ribs. The ribs are wrapped around the center hub during storage time and at deployment time, it reverts to its original shape due to the rigidity of the rib. The deployment mechanism steps can be seen in Fig. 6a and b. It is a one-time sequence where the antenna unfolds into a deployed state. For such, very flexible spring ribs were designed for adequate bending in order to tolerate tensions until deployment.

Each rib is a parabolic strip cut out from a spring steel plate. In order to ascertain restoring forces, material properties such as flexibility and rigidity of strip cuts with various configurations were analyzed. Since the rigidity of a single plate is insufficient, making it difficult to wind it around the main hub, a “sandwich” structure is adopted, in which a honeycomb rubber core is placed between two plates. Therefore, with rubber cores discretely arranged along the ribs, rigidity is improved so that the surface plate can tolerate tensions when bent, retaining the shape of the parabolic reflector after deployment.

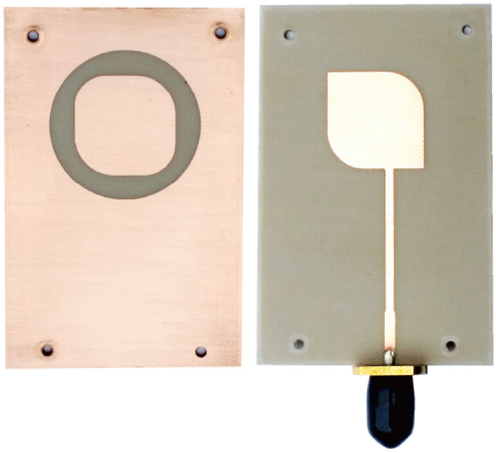

Fig. 4. Constructed microstrip antenna shown in separate parts.

3. Antenna gain estimation

The maximum achievable gain (G_{max})of a parabolic reflector

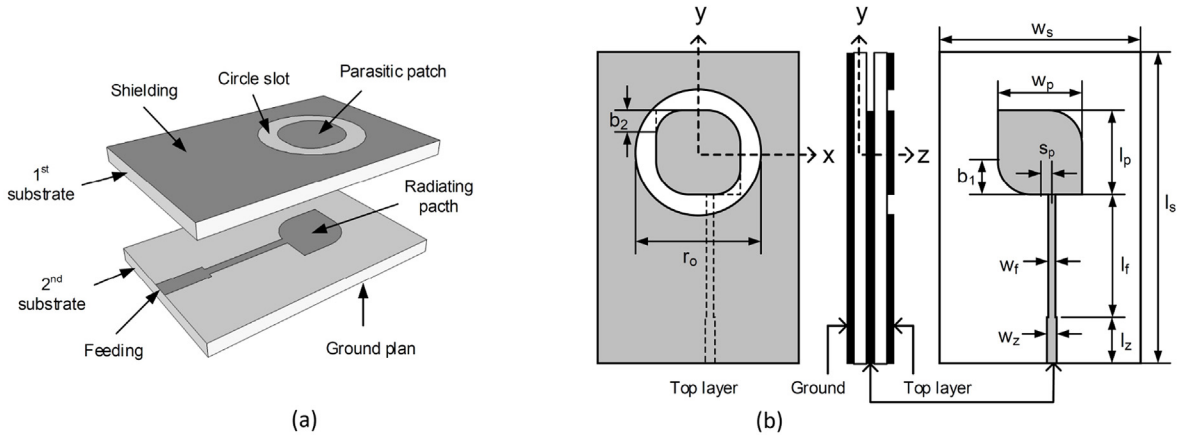

Fig. 3. Configuration of the designed feed antenna. (a) 3D view; (b) detailed geometry.

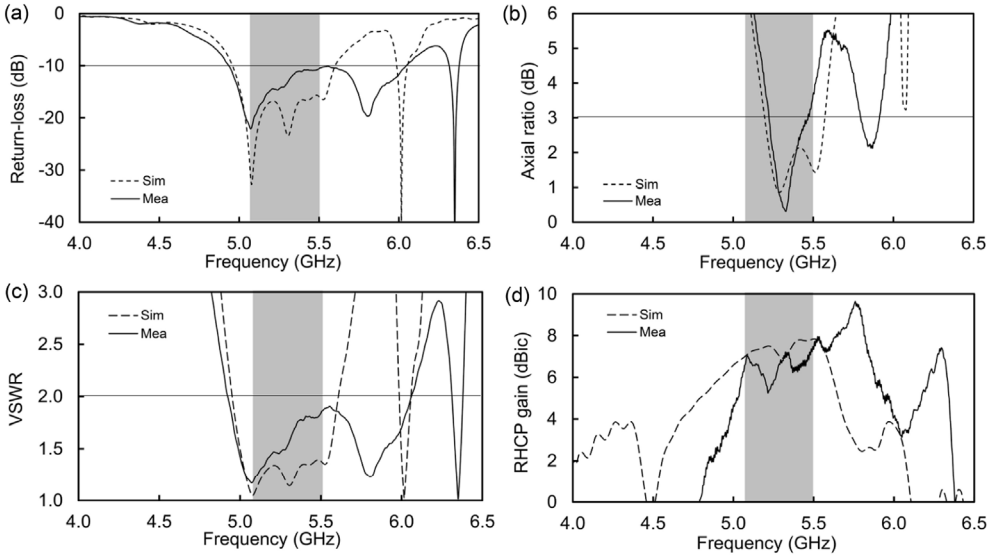

Fig. 5. Simulated and measured performance of microstrip feed antenna regarding: (a) return-loss; (b) axial-ratio; (c) Voltage Standing Wave Ratio (VSWR); (d) gain.

Table 3
Main performance parameters of microstrip feed antenna. Gain, axial ratio and cross-polarization were measured at $f_c$and boresight.

Parameter	Performance
Gain	7.1 dBic
Axial ratio bandwidth	4.7%
Impedance bandwidth	20.9%
Half-power angle	75. 6°
10-dB angle	147°
Axial Ratio	0.88 dBic
Cross-polarization	−18.9 dBic

antenna is given by $\left(\frac{\pi D}{\lambda}\right)^2$, which in this case is 46.01 dBic. The actual gain is in fact $G = \eta G_{max}$, where η is the overall antenna efficiency given by Ref. [15], which accounts several factors, such as impedance mismatch, antenna aperture, reflector surface roughness, among others. These contributions must be estimated for calculating the antenna effective gain. Apart from peak loss, antenna sidelobes must be carefully controlled, as they can increase range ambiguities, degenerating the final image. For the CP-SAR, sidelobe levels must be below −20 dB.

3.1. Perfect parabolic reflector

In order to identify losses introduced by the different elements of the antenna system, the reflector is first optimized for its center frequency, considering a perfect parabolic surface without ribs or feed assembly. A theoretical feed pattern of form $cos^n(\theta)$was used for the design optimization, with −10 dB edge taper. The feed, located at the paraboloid focal point, spreads spherical waves as $\frac{1}{r}$, where r is the distance from the focus to the reflector. These spherical waves are transformed by the paraboloidal reflector into a plane wave propagated to the aperture plane at a constant amplitude.

A theoretical pattern for a circularly polarized feed [16] can be described by

$$E(r) = A_0 e^{j\tau\phi}[\hat{\theta}C_E(\theta) + \hat{\phi}j\tau C_H(\theta)]\frac{e^{-jkr}}{r} \tag{2}$$

where $A_0$is a complex constant, $\tau = +1$for LHCP or $\tau = -1$for RHCP, and

$$C_E(\theta) = C_H(\theta) = cos^n(\theta) \tag{3}$$

for $0 < \theta < \frac{\pi}{2}$ in the E- and H-plane patterns, respectively. The parabolic half-angle $\theta_0$is defined as $2\tan\left(\frac{1}{4\frac{f}{D}}\right) = 69.39°$. The variable n relates to the feed illumination taper T in [dB] and θ_0, given by:

$$n = \frac{-0.05.\ T}{log\left[cos\left(\frac{\theta_0}{2}\right)\right]} \tag{4}$$

Ignoring any central blockage, spillover efficiency (η_{spill}) and amplitude taper efficiency (η_{taper}) are calculated as:

$$\eta_{spill} = 1 - u^{2(n+1)} \tag{5}$$

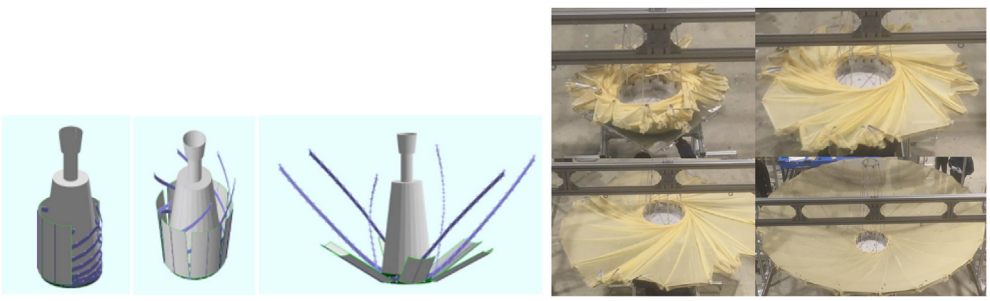

(a) (b)

Fig. 6. Wrap-rib deployment: (a) conceptual mechanism, and (b) deployment test.

$$\eta_{taper} = \frac{4(n+1)(1-u^n)^2}{n^2[1-u^{2(n+1)}]}\cot^2\frac{\theta_0}{2} \quad (6)$$

where $u = cos\left(\frac{\theta_0}{2}\right)$.

For an ideal −10 dB edge taper feed, amplitude taper and feed illumination efficiency values are $\eta_{taper} = \eta_{spill} = -0.457$dB. As for feed blockage losses, they occur around the boresight of the reflector where the field is shadowed by the feed platform. This blocking causes an increase of the SLL due to the discontinuous aperture distribution and the scattering of the incoming wavefront by the blocking structure. Minimizing central blockage requires smaller feed systems. Effect on cross-polarization, axial ratio and sidelobes are studied by modelling a blocking disk with varying radius placed at the parabolic focal point. In order to keep sidelobe levels values below −25 dB, maximum dimension of the feed blockage has to be no larger than 28.8 cm, with respective $\eta_{block} = 0.11$dBic.

The microstrip feed used has largest dimension of 7.8 cm, which gives almost negligible blockage losses of 0.002 dB, and losses η_{taper}, $\eta_{spill}$of 2.26 dBic for an ideal parabolic reflector.

3.2. Effect of ribs

Next, losses regarding the effect of ribs and subsequent quasi-parabolic surface are estimated using the microstrip antenna as feed element. The reflector has supporting ribs that are parabolic in shape and wire mesh stretched between them; that means that the surface between 2 ribs is a quasi-parabolic area. This gore shape causes phase error loss and their periodicity produces extra sidelobes. Consequently, the focal point of the parabola becomes a spread focal region, within where the feed position has to be optimized to minimize the phase error over the surface [17]. The optimization process is based on numerical simulation by analyzing the feed position with regards to the respective phase losses. From the parametric results using the full wave simulation program, the new feed location that minimizes peak gain loss is at +1.5 cm from the focal point after optimization. Ideally this position also has to be verified and adjusted empirically, given actual gore shape and reflector surface distortions, however this approach was not feasible in these measurements, so the feed position referred here is derived from the simulations only. Equation (7) calculates the minimum number of gores $N_G$for a given antenna diameter D, f/D ratio, wavelength λ, and peak-to-peak phase deviation δ across the gore [18]. As the number of ribs increases, phase error losses decrease, as the surface becomes closer to a perfect paraboloid. For the current parabolic configuration, using a 10-dB taper feed, at least 21 ribs are needed to keep gore losses below 0.5 dB.

$$N_G = \sqrt{\frac{800 - 500\left(\frac{f}{D} - 0.4\right)}{\delta}\frac{D}{\lambda}} \quad (7)$$

When accounting other factors than antenna losses, such as mechanical stability, risk of deployment failure and stowage space, 24 supporting ribs were estimated necessary. After simulating the antenna pattern accounting ribs and gore surface, there was no significant impact on the shape of the main pattern, with peak losses of $\eta_{ribs} = 0.03dB$and a slight increase in the sidelobes to −37.6 dB.

3.3. Effect of mesh reflectivity

The reflector antenna surface is composed of a fine knitted mesh wire of 28 openings per inch (OPI), molybdenum core diameter of 30 μm and gold-coated surface of 0.2 μm. The small wire diameter together with the excellent RF conditions and softness of the gold plating creates low wire-to-wire contact resistance, which is essential for maintaining good RF performance. The mesh type adopted is woven in a single wire, namely, single atlas pattern, as seen in Fig. 7b. Given the proportions of reflector dimensions and mesh opening size, where mesh opening sizes are 57 times smaller than the center wavelength, computer simulation of the mesh parabolic reflector in C-band frequencies becomes an impossible task. For that reason, the parabolic reflector is assumed solid in antenna simulations, and reflectivity loss $\eta_R$is then estimated by measuring the shielding effectivity of the mesh sample when placed between two identical horn antennas, as detailed in Ref. [19]. Assuming negligible dissipation losses in the mesh, reflectivity loss is then estimated in the center frequency by $\eta_R = 0.0027$dB.

3.4. Effect of struts

Support struts block the aperture of a centrally fed reflector and reduce antenna gain. Because the passing waves induce currents on the struts that radiate, the effect of struts can be larger than their area. The struts have circular cross-section of 10 mm diameter and length of 1.308 m and are illuminated by spherical waves from the feed. Induced currents together with the feed illuminate the reflector. Each strut creates a shadow on the field generated by the feed, which decreases the spillover for θ larger than zero. A parametric analysis of the effect of number of struts on the radiation pattern is performed, and six main aluminum struts were chosen as they provide good compromise between mechanical stability of the structure and acceptable levels of peak amplitude losses (0.4 dB) and SLL (−31.5 dB) for an ideal feed.

However, simulated results with the microstrip antenna as feed show high peak losses of $\eta_{struts} = 4.47dBic$, a considerate increase in sidelobe levels and axial ratio degeneration to levels above specification. That can be attributed to the struts scattering and diffraction effects on the microstrip's radiation pattern, differing from an ideal 10-dB pattern with axial ratio <1, taper angle exceeding in few degrees and main lobe deviating 1–2° from boresight. Therefore, careful design of feed assembly must be conducted in order to achieve a high level of circular polarization purity and a radiation pattern as close to a 10-dB-taper as possible. Sidelobe levels control is most critical for SAR applications, and although SLL still remain within specified levels, further considerations regarding the strut geometry for better overall RF performance are also being carried out. But for validation purposes of the parabolic mesh reflector, the microstrip simulation results as feed antenna are acceptable.

Fig. 8a and b illustrate the effects of the quasi-parabolic surface and struts. Table 4 summarizes the main contributions affecting the antenna radiation pattern, with total antenna efficiency estimated in $\eta_{total} = 6.94$dB.

4. Validation of parabolic mesh reflector

4.1. Verification of surface error

Reflector surface errors, due to fabrication errors, deformations caused by gravity, or roughness of the reflective surfaces, reduce the antenna gain estimated. Antenna surface tolerances were limited to 3.5 mm following Ruze's prediction for surface tolerance efficiency of 3 dB.

A research model of the deployable parabolic mesh reflector was constructed, as depicted in Fig. 7a. Two approaches to measure surface accuracy of the mesh reflector using laser and three-dimensional photogrammetric technique were performed.

4.1.1. Laser measurements along ribs

With the parabolic reflector facing upwards, a reference plane is placed below it, and fixed points along each of the 24 ribs were measured with a laser meter that can be displaced along the reference place. 11 points distanced 10 cm from each other were marked with reflective tapes. These points were marked on each rib's lateral, i.e., along its right and left side. Misalignment errors are included in overall surface error. RMS surface error is computed as the RMS difference between theoretical value of parabolic rib shape and measured values. Results show

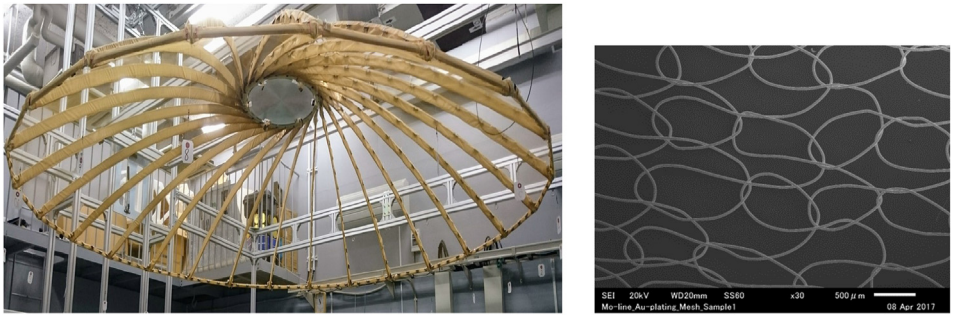

(a) (b)

Fig. 7. (a) Research model of deployable parabolic mesh reflector antenna. (b) Close-up of mesh woven in single atlas pattern.

average RMS error of 1.92 mm ± 1.125mm on the right side of the rib and 1.93 mm ± 0.53mm on the left side of the rib, both below the required 3.5 mm RMS surface error.

4.1.2. 3–D scanning of mesh reflector surface

In order to scan the reflector surface, the photogrammetric device was placed 2 m away from the center of parabolic reflector. A commercial 3D scanning device was used for reflector contour measurement [20]. 11 overlapping images composed of triangular mesh cells were generated, covering the reflector surface area with spatial resolution of 1 mm. In order to avoid background scattering from the surroundings, an anti-reflective sheet was placed behind the reflector. The measurements showed that, although detectable, the thin mesh material scatters the projected light more than it reflects back towards the camera, resulting in very noisy surface estimations. Since the ribs presented clear shape, they were then used as measured reference for reflector shape. Each scan then was converted into a point cloud of 2,500,000 points. Noise and artifacts were removed and filtered. Each point cloud scan was then directly compared with the theoretical parabolic surface using a best fit function, and these distances computed as errors. Cloud-to-cloud (C2C) distances computations were based on a quadratic function. A surface map of calculated C2C distances using the k-nearest neighbor classifier can be seen in the color map displayed in Fig. 9. Standard deviation *std* and mean μ of the normal distribution of C2C distances are computed, with overall RMS error of 3.86 mm ± 2.36.

4.2. Near-field antenna measurements

Antenna pattern measurements were realized with a near-field plane polar system at A-METLAB facilities at Kyoto University, composed of a robot scanner, a dual-linearized probe, and a computer subsystem. From the sampled radiating near-field, the data can be later converted into far-field. The measuring probe is located in the ceiling, and the antenna under test (AUT) on a lifting table over a turn plane on the ground. Fig. 10a and b illustrates the planar near-field measurement system setup. The distance from probe to AUT was 0.79 m. The probe gathered 247 points along a radius of 6.36 m at 0.026 m spacing, and 376 points on a polar fashion at 0.48°step. Far-field points were generated, 1201 points in the azimuth and elevation directions, ranging from − 60°to + 60°, at step angle of 0. 1°. Results are depicted in Fig. 11, showing simulated and measured far-field antenna radiation pattern in co-polarization, cross-polarization and axial ratio at center frequency. Directivity measured was 40.6 dBic, with peak slightly deviated from the boresight by 0.727°. Highest measured SLL was 22.68 dB, and axial ratio 3.3 dBic at center frequency. A summary of simulated and measured results are in Table 5. From the near-field measurements, holographic maps were also derived, displaying amplitude and phase data of co-polarization field in Fig. 12.

Table 4
Illumination losses at 5.3 GHz: effect of antenna elements on radiation pattern in units of decibels. For surface accuracy losses, the measured 1.92 mm RMS is considered in Ruze's equation.

	Co-Pol	Peak Loss	Peak SLL
Ideal parabolic	46.0	–	–
Spillover, taper	43.7	2.26	−41.5
Mesh	–	0.0027	–
Surface Accuracy	–	0.185	–
Gore shape	43.7	0.03	−37.6
Struts	39.3	4.47	−20.0
Total	39.1	6.94	−20.0

5. Discussion

Since the mesh material is fixed on the reflector structure by being

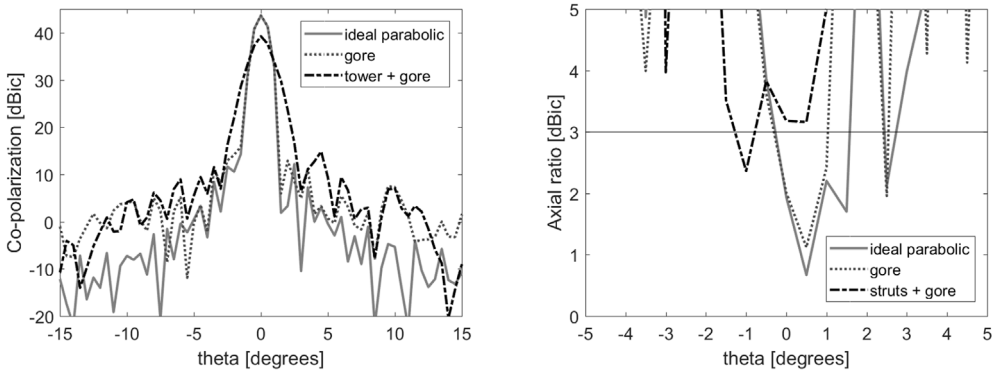

(a) (b)

Fig. 8. Simulated antenna pattern radiation accounting different elements contribution at center frequency and H-plane ($\phi = 90°$). All values are in units of decibels.

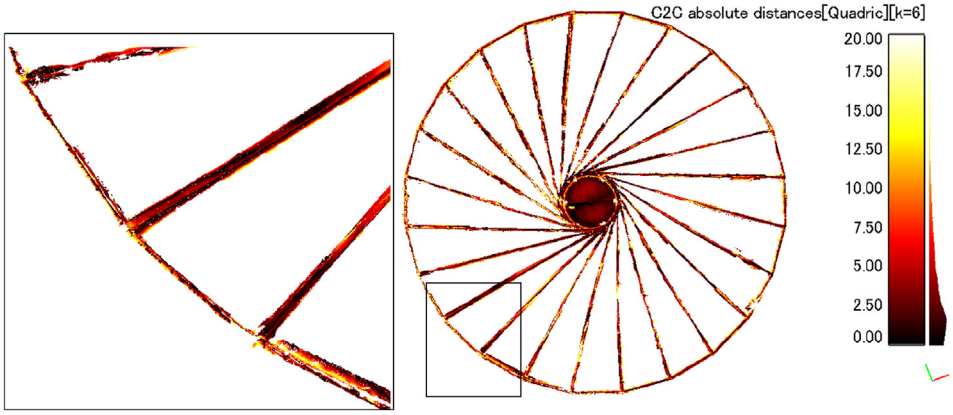

Fig. 9. Computed cloud-to-cloud (C2C) absolute distances in millimetres between reflector model and scanned areas of reflector ribs, rims and center plate.

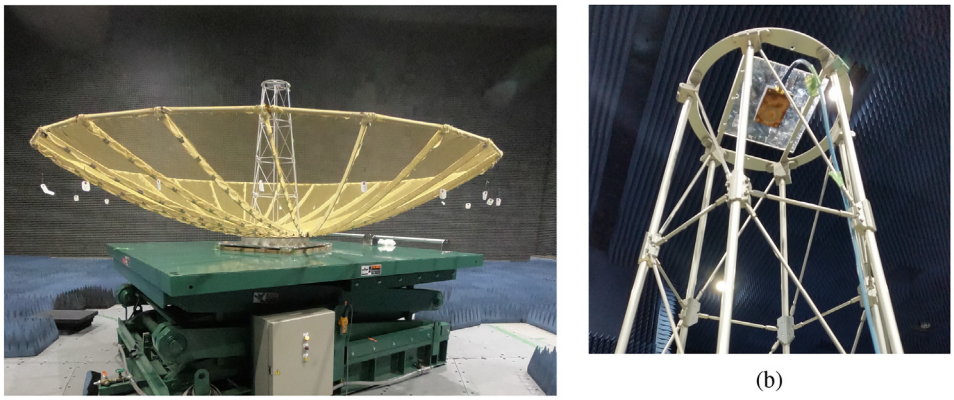

Fig. 10. (a) Parabolic reflector over lifting table for near-field measurements. (b) Close-up of feed tower.

stretched and stitched around ribs and rims, there is an added volume of mesh material over these structures. Hence, in both measurement methods for geometric surface verification, some deviation from the theoretical model is expected. Additionally, the reflector position in each measurement setup was different; in the laser measurement, the reflector was facing upwards, whereas in the 3D scanning measurement setup, it was facing almost horizontally. Therefore, reflector surface distortions due to gravity are also expected to be different in each measurement setup. Results from the laser measurements presented largest discrepancy from rib number 9, with 3.6 mm RMS, but overall ribs measurements presented 1.92 mm RMS, lower than the required surface accuracy of 3.5 mm RMS. The 3D scanning results, on the other hand, presented higher RMS error of 3.86 mm. This difference in surface accuracy error can be attributed to the low image SNR of mesh material when 3D scanned, possible image misregistration of scanned patches, and more significant reflector distortion due to gravity compared to the laser setup. In the future, errors in the image processing steps can be reduced by using geo-referenced reflective tags on the parabolic surface under the same 3D scanning approach. For estimation of surface accuracy losses, the measured 1.92 mm RMS is used in Ruze's equation [21], as this value is less prone to measurement errors. The gain table presented in Table 4 includes this calculated loss value.

Far-field results derived from the near-field antenna pattern measurement showed very good agreement between simulation and measured data in both azimuth and elevation planes. Measured peak directivity is 39.5 dB, with highest peak sidelobe of −20.96 dB. Measured axial ratio also agreed with simulations, although in both cases, the axial ratio at boresight presented slightly higher values than the required 3 dB, due to mostly scattering from the tower struts, as previously mentioned in Section 3.4.

Fig. 12a is a holographic amplitude map at the antenna aperture, which can be interpreted as the illumination efficiency of feed on the main reflector. The amplitude map also shows a feed taper ranging from −20 to −25 dBic along reflector rims, close to the simulated microstrip pattern, with taper of −24 dB and −28 dB at − 69°and + 69°. It also shows an unevenly spread illumination, with radial areas more highlighted than the rest of the surface, suggesting that the reflectivity of the knitted mesh is not as high as the ribs' for circularly polarized waves in the C-band frequencies. Although there is little degeneration of axial ratio, co- and cross-polarization levels at boresight, as referred in Table 5, differences in the shape of measured and simulated results in Fig. 11 can be attributed to these mesh effects to the propagating wave, since in the simulations, the reflector was assumed rigid. Adopting a mesh type with a pair of wires, as in the single satin mesh type, instead single wires can reduce the variance of reflectivity dependant on the direction of electric field of the incident wave. Although single satin mesh type has been previously reported to have superior electrical performance compared to the single atlas type for CP applications [22], measured frequencies were conducted at 20 GHz in the reported experiment. Hence, further investigations on the mesh reflectivity for CP waves in the C-band must be carried out. Other inhomogeneous areas in the amplitude map can also be a result of an improperly focused antenna, multiple reflections, diffraction effects due to struts and other elements, reflector surface distortions and potential misalignment in the setup. Precise alignment between probe and AUT was difficult due to mechanical vibrations from the lifting table when used, which could have resulted in slight movements of the antenna configuration.

The holographic phase map gives a good approximation of surface distortions, and jumpy phases of ± 180°can be seen as the phase is still wrapped. Although the generated phase hologram is not focused over

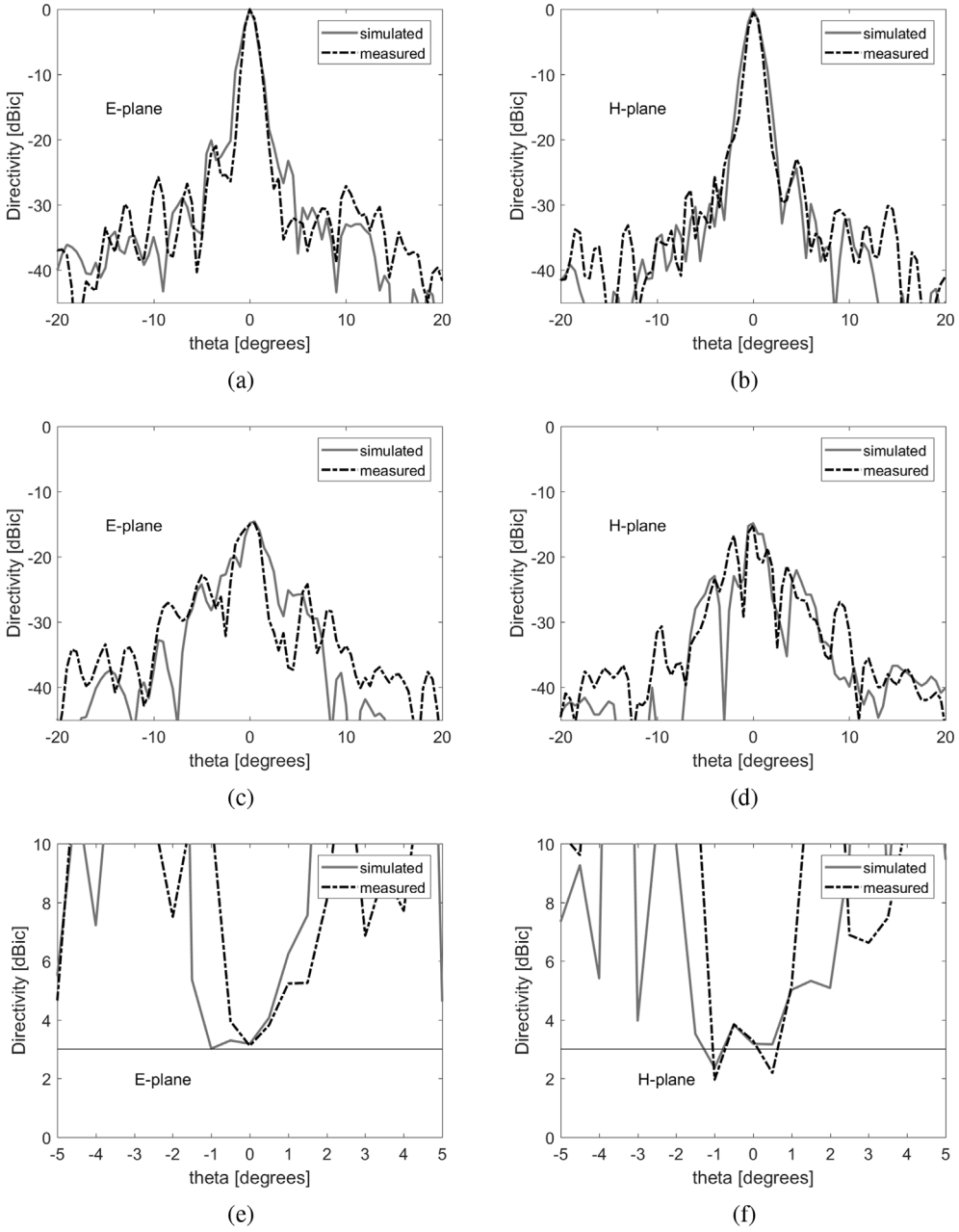

Fig. 11. Simulation and measurement results at center frequency of normalized co-polarization levels in the (a) E-plane, (b) H-plane; cross-polarization levels in the (c) E-plane, (d) H-plane; axial ratio in the (e)E-plane, (f) H-plane.

Table 5
Results of near-field antenna measurements at center frequency: peak co-polarization at boresight, axial ratio (AR), half-power angle (3 dB BW), sidelobe levels (SLL) and cross-polarization at boresight (X-pol) in dBic.

	Co-pol	AR	3 dB BW	SLL	X-pol
Measured	39.5 dBic	3.2 dBic	1. 2°	−20.9 dB	25.0 dBic
Simulated	39.3 dBic	3.1 dBic	1. 3°	−20.1 dB	24.4 dBic

the reflector surface at all points, it still gives an idea of surface errors. Again, the ribs and other elements appear to affect the phase distribution; additionally, a visible difference in phase and amplitude at the bottom-right quarter of the reflector can be seen, which could be attributed to a possible tilt of the reflector platform plane.

Validation of the deployable mesh parabolic reflector presented overall good results, but further analysis on the strut design must be conducted to minimize scattering effects, as previously described. Additionally, future work should focus on the development of the feed assembly for a full polarimetric configuration, and later tested with the reflector.

6. Conclusion

This paper describes the design and development status of a compact CP-SAR system compatible to a 150-kg class satellite. Small satellites introduce a new realm of options given their low costs and reduced manufacturing time of spacecraft platforms, becoming very attractive alternatives to traditional remote sensing missions.

The C-band CP-SAR microsat is a technology demonstrator and compact science mission for disaster mitigation using C-band CP-SAR developed by Chiba University and LAPAN. The key technology for a compact design is mainly based on the SAR antenna; the antenna is of

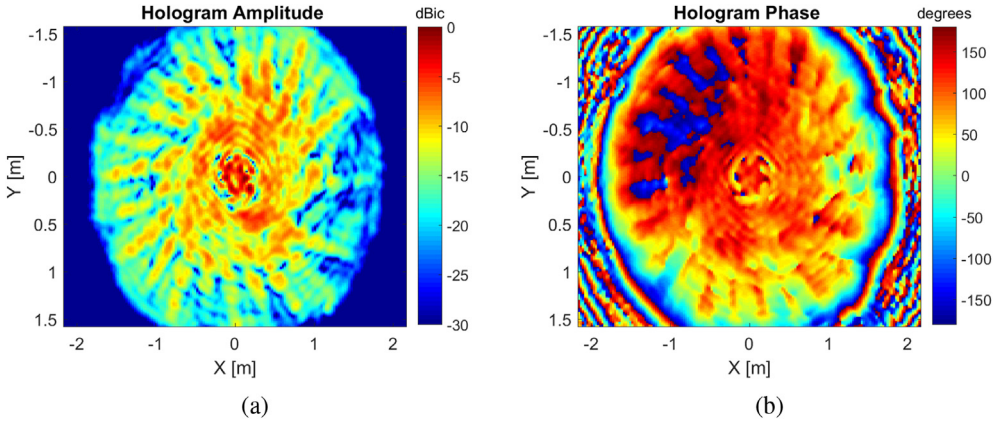

Fig. 12. Hologram at aperture level in center frequency of (a) field amplitude and (b) phase.

deployable type, with total mass less than 15 kg and carefully designed to fit piggy-back volume and weight constrains. The deployable reflector is a center-fed parabolic mesh with diameter of 3.6 m.

In this work, mission specification and overall design parameters were presented, justifying the use of the deployable mesh parabolic reflector in the current mission. Simulations and measurements of antenna radiation were presented, with contributions of different antenna elements to the final radiation pattern. Antenna surface estimation was realized by two approaches: 1) using a laser distance meter along ribs, and 2) scanning the reflector surface with a 3D scanning device. In both methods, RMS error is achieved by direct comparison with theoretical parabolic shape, with respective values of 1.92 mm and 3.86 mm. Near-field antenna measurements confirmed good agreement with simulation of parabolic mesh reflector.

For future work, more accurate reflector surface distortion information shall be extracted, derived from the holographic phase information, as well as further analysis of the effects of critical parameters to the RF performance in the C-band, and finally, prototyping/testing the feed assembly.

Acknowledgment

This work is supported by the Japanese Government National Budget Ministry of Education and Technology (MEXT) FY2015-2017 under Grant 2101, and Chiba University Strategic Priority Research Promotion Program FY2016-FY2018.

The authors also thank the research group colleagues Dr.Chua Ming Yam, Peberlin Sitompul, Mirza M. Waqar, and collaborator Prof. Shinohara from Kyoto University for their kind support.

Appendix A. Supplementary data

Supplementary data to this article can be found online at https://doi.org/10.1016/j.actaastro.2019.01.030.

References

[1] S. Gao, K. Clark, M. Unwin, J. Zackrisson, W.A. Shiroma, J.M. Akagi, K. Maynard, P. Garner, L. Boccia, G. Amendola, G. Massa, C. Underwood, M. Brenchley, M. Pointer, M.N. Sweeting, Antennas for modern small satellites, IEEE Antenn. Propag. Mag. 51 (4) (2009) 40–56, https://doi.org/10.1109/MAP.2009.5338683.

[2] K. Ouchi, Recent trend and advance of synthetic aperture radar with selected topics, Rem. Sens. 5 (2) (2013) 716–807, https://doi.org/10.3390/rs5020716 http://www.mdpi.com/2072-4292/5/2/716.

[3] U. Naftaly, R. Levy-Nathansohn, Overview of the TECSAR satellite hardware and mosaic mode, IEEE Geosci. Remote Sens. Lett. 5 (3) (2008) 423–426, https://doi.org/10.1109/LGRS.2008.915926.

[4] J. Korczyk, Reliable on Board Data Processing System for the Iceye-1 Satellite, Master's thesis, KTH, School of Information and Communication Technology (ICT), 2016.

[5] C. M. Yam, C. E. Santosa, J. T. S. Sumantyo, The Maiden Flight of Hinotori-C: the first C band full polarimetric circularly polarized synthetic aperture radar in the world, IEEE Aerospace Electronic Systems Magazine.

[6] T. Motohka, Y. Kankaku, S. Suzuki, Advanced land observing satellite-2 (alos-2) and its follow-on l-band sar mission, IEEE Radar Conference, 2017 RadarConf), 2017, pp. 0953–0956, , https://doi.org/10.1109/RADAR.2017.7944341.

[7] M. Mobrem, S. Kuehn, C. Spier, E. Slimko, Design and performance of astromesh reflector onboard soil moisture active passive spacecraft, IEEE Aerospace Conference, 2012 2012, pp. 1–10, , https://doi.org/10.1109/AERO.2012.6187094.

[8] M.W. Thomson, The astromesh deployable reflector, IEEE Antennas and Propagation Society International Symposium. 1999 Digest. Held in Conjunction with: USNC/URSI National Radio Science Meeting (Cat. No.99CH37010), 3 1999, pp. 1516–1519, , https://doi.org/10.1109/APS.1999.838231 vol. 3.

[9] P.R. Akbar, J.T.S. S, H. Kuze, A novel circularly polarized synthetic aperture radar (cp-sar) system onboard a spaceborne platform, Int. J. Rem. Sens. 31 (4) (2010) 1053–1060, https://doi.org/10.1080/01431160903156528.

[10] R.K. Raney, Hybrid-quad-pol sar, IGARSS 2008 - 2008 IEEE International Geoscience and Remote Sensing Symposium, 4 2008, https://doi.org/10.1109/IGARSS.2008.4779765 pp. IV – 491–IV – 493.

[11] Y. Izumi, S. Demirci, Z. Baharuddin, J. Sri Sumantyo, H. Yang, Analysis of circular polarization backscattering and target decomposition using gb-sar, Progress In Electromagnetics Research B 73 (2017) 17–29, https://doi.org/10.2528/PIERB16081701.

[12] J. Llop, P. Roberts, Z. Hao, L. Tomas, V. Beauplet, Very low earth orbit mission concepts for earth observation: benefits and challenges, Reinventing Space Conference, 2014.

[13] D. Systemes, CST - Computer Simulation Technology. URL https://www.cst.com.

[14] C.E. Santosa, J.T.S. Sumantyo, K. Urata, M.Y. Chua, K. Ito, S. Gao, Development of a low profile wide-bandwidth circularly polarized microstrip antenna for c-band airborne cp-sar sensor, Progress In Electromagnetics Research C 81 (2018) 77–88, https://doi.org/10.2528/PIERC17110901.

[15] P. Kildal, Factorization of the feed efficiency of paraboloids and cassegrain antennas, IEEE Trans. Antenn. Propag. 33 (8) (1985) 903–908, https://doi.org/10.1109/TAP.1985.1143689.

[16] S.K. Sharma, S. Rao, L. Shafai, Handbook of Reflector Antennas and Feed Systems: v.1 Theory and Design of Reflectors, Artech House, Norwood, 2013http://cds.cern.ch/record/2105300.

[17] P. Ingerson, W. Wong, The analysis of deployable umbrella parabolic reflectors, Antennas and Propagation Society International Symposium, 8 1970, pp. 18–20, , https://doi.org/10.1109/APS.1970.1150810 1970.

[18] T.A. Milligan, Modern Antenna Design, McGraw-Hill, Inc., New York, NY, USA, 1985.

[19] K.P.I.T. Center, Shielding Effectivity Measurement Method above 1 Ghz, (2014) https://www.kanagawa-iri.jp/wp/wp-content/uploads/filebase/reports_of_research/H26/65_Note16.pdf.

[20] G. DAVID, SLS-2 User Manual, (2012).

[21] J. Ruze, Antenna tolerance theorya review, Proc. IEEE 54 (4) (1966) 633–640, https://doi.org/10.1109/PROC.1966.4784.

[22] A. Miura, M. Tanaka, A mesh reflecting surface with electrical characteristics independent on direction of electric field of incident wave, IEEE Antennas and Propagation Society Symposium, 1 2004, pp. 33–36, , https://doi.org/10.1109/APS.2004.1329546 2004 Vol.1.